










# Detection of a Type-C QPO during the soft-to-hard transition in Swift J1727.8–1613

Maïmouna Brigitte<sup>★</sup><sup>1,2</sup>, Noel Castro Segura<sup>3</sup><sup>3</sup>, Federico García<sup>4,5</sup><sup>4,5</sup>, Jiří Svoboda<sup>1</sup><sup>1</sup>, María Díaz Trigo<sup>6</sup><sup>6</sup>,  
Mariano Méndez<sup>7</sup><sup>7</sup>, Federico Vincentelli<sup>8</sup><sup>8</sup>, Douglas J. K. Buisson<sup>9,10</sup><sup>9,10</sup>, and Diego Altamirano<sup>11</sup><sup>11</sup>

<sup>1</sup> Astronomical Institute of the Czech Academy of Sciences, Boční II 1401/1, 14100 Prague 4, Czech Republic

<sup>2</sup> Astronomical Institute, Faculty of Mathematics and Physics, Charles University, V Holešovičkách 2, Prague 8, 18000, Czech Republic

<sup>3</sup> Department of Physics, University of Warwick, Gibbet Hill Road, Coventry CV4 7AL, UK

<sup>4</sup> Instituto Argentino de Radioastronomía (CCT La Plata, CONICET; CICPBA; UNLP), C.C.5, (1894) Villa Elisa, Buenos Aires, Argentina

<sup>5</sup> Facultad de Ciencias Astronómicas y Geofísicas, Universidad Nacional de La Plata, Paseo del Bosque, B1900FWA La Plata, Argentina

<sup>6</sup> ESO, Karl-Schwarzschild-Strasse 2, 85748, Garching bei München, Germany

<sup>7</sup> Kapteyn Astronomical Institute, University of Groningen, PO BOX 800, Groningen NL-9700 AV, the Netherlands

<sup>8</sup> INAF Istituto di Astrofisica e Planetologia Spaziali, Via del Fosso del Cavaliere 100, I-00133 Roma, Italy;

<sup>9</sup> Department of Physics and Astronomy, University of Southampton, Highfield, Southampton, SO17 1BJ

<sup>10</sup> Institute of Astronomy, University of Cambridge, Madingley Road, Cambridge, CB3 0HA

<sup>11</sup> School of Physics and Astronomy, University of Southampton, Highfield, Southampton, SO17 1BJ, UK

Received date Accepted date

## ABSTRACT

**Context.** Timing analysis of accreting systems is key to probe the structure and dynamics around compact objects. In Black-Hole Low-Mass X-ray Binaries (BH LMXBs), the compact object accretes matter from a low-mass companion star via Roche Lobe overflow, forming an accretion disk, and occasionally exhibiting bright eruptions. The BH LMXB *Swift* J1727.8–1613 (hereafter *J1727*), recently underwent one of the brightest outbursts ever recorded in X-rays, in August 2023.

**Aims.** This analysis aims to study the timing properties of *J1727*, in the decaying phase of its outburst, using high-time resolution *XMM-Newton* data.

**Methods.** We analyzed *J1727*'s power spectrum (PS) and cross spectrum (CS), which we modeled with Lorentzians. The PS reveals how the source's power is distributed across frequencies, and the Real and Imaginary parts of the CS compare the displacement of the light curves in different energy bands across the observations. Finally, we simultaneously derived the phase lags and the coherence, using a constant phase lag model.

**Results.** While the first (soft-state) observation does not show any strong variability, the two harder observations exhibit quasi-periodic oscillations (QPOs). Because the QPO is more significantly detected in the Imaginary part of the CS than in the PS, we refer to it as the "Imaginary QPO". The QPO is more prominent in the soft 0.3–2 keV band than in the hard 2–12 keV band. As the source evolves towards the hard state, the Imaginary QPO shifts to lower frequencies, the broadband fractional rms amplitude in the 0.3–2 keV energy band increases, while the rms covariance of the Imaginary QPO decreases. Simultaneously, the phase lags increase and the coherence function drops at the Imaginary QPO frequency.

**Conclusions.** In the elusive soft-to-hard transition of *J1727*, the first *XMM-Newton* observations of the source reveal an Imaginary QPO also detected in the PS, exhibiting the properties of a type-C QPO.

**Key words.** Stars: black holes – X-rays: binaries – X-rays: individual: Swift J1727.8–1613

## 1. Introduction

Black hole Low-Mass X-ray Binaries (BH LMXBs) consist of a black hole accreting matter from a low-mass companion star through Roche Lobe overflow (Frank et al. 2002). Several of these sources display outbursts, during which their flux increases by a few orders of magnitude over a few weeks to months (Zdziarski et al. 2004; Done et al. 2007; Hirsch et al. 2020). The spectral and timing properties of these sources exhibit dramatic changes throughout the outburst evolution, transitioning from the Hard state (HS) to the Soft state (SS; Remillard & McClintock 2006). In the HS, the emission from the hot Comptonized

medium (often referred to as the "corona") dominates the X-ray spectrum. In contrast, during the SS, a multi-blackbody emission from the accretion disk dominates the high-energy spectrum (see Shakura & Sunyaev 1973). The transition between these two spectral states is often referred to as the hard-intermediate state (HIMS) and the soft-intermediate state (SIMS; Belloni et al. 2005), which are less commonly observed than the HS and the SS, because of their short lifespan (Dunn et al. 2010). *Swift* J1727.8–1613 (hereafter *J1727*), is one of the few sources observed in the decaying phase of the outburst. First detected on August 24, 2023 (Dichiara et al. 2023; Negoro et al. 2023), the source's emission peaked at around 7 Crabs in the 2–20 keV energy band, exhibiting an exceptionally bright outburst. *J1727*

★ E-mail: maimouna.brigitte@asu.cas.cz

is the first BH LMXB observed with the Imaging X-ray Polarimetry Explorer (IXPE; Weisskopf et al. 2022) across the entire outburst – from the brightening in the hard state (Veledina et al. 2023), through the hard-to-soft transition (Ingram et al. 2024), to the soft state (Svoboda et al. 2024), and finally in the dim hard state (Podgorný et al. 2024). Optical spectroscopy during quiescence suggests the presence of a black hole primary (Mata Sánchez et al. 2024), located at  $5.5_{-1.1}^{+1.4}$  kpc (Burridge et al. 2025), defining the system as a Low-Mass X-ray Binary (LMXB; Castro-Tirado et al. 2023).

Throughout the outburst – traced by a "q" shape in the hardness intensity diagram (HID; e.g. Homan et al. 2001; Fender et al. 2004) – transient BHXBs exhibit fast X-ray variability. Quasi-periodic oscillations (QPOs; van der Klis 1989; Psaltis et al. 1999; Belloni et al. 2002; Giannios & Spruit 2004) are among the components that can be tracked during an outburst, providing insight into the inner parts of the system. Low-Frequency QPOs (LFQPOs) are the most commonly observed, with frequencies ranging from  $\sim 0.01$  Hz to  $\sim 30$  Hz (Norris & Wood 1987; Wijnands & van der Klis 1998; Casella et al. 2004; Belloni et al. 2005). Based on the strength of the broadband variability and QPO characteristics, LFQPOs can be classified into three main types: Type-A, -B and -C (Casella et al. 2005).

Type-C QPOs are characterized by a strong and narrow peak in the power spectra (PS). The observed fractional root mean square (rms) amplitude ranges from 15% to 30%, and the QPO appears simultaneously with strong broadband variability (Casella et al. 2004; Belloni et al. 2005). The origin of these QPOs remains an open question. Nevertheless, the leading suspects proposed in different models are instabilities in the accretion flow (Tagger & Pellat 1999; Titarchuk & Fiorito 2004; Mondal et al. 2009), geometrical effects due to the Lense–Thirring precession (Stella & Vietri 1998; Stella et al. 1999; Ingram et al. 2009; Kubota et al. 2024), time-dependent Comptonization (García et al. 2021; Mastichiadis et al. 2022; Bellavita et al. 2022), and a precessing jet (Ma et al. 2021). Type-C QPOs were detected in the HIMS of *J1727* with different X-ray telescopes such as the *Neil Gehrels Swift Observatory* (Palmer & Parsotan 2023), the *Neutron Star Interior Composition Explorer* (NICER; Draghis et al. 2023; Bollemeijer et al. 2023; Liao et al. 2024; Rawat et al. 2025), *Insight-Hard X-ray Modulation Telescope* (*Insight-HXMT*; Yu et al. 2024; Chatterjee et al. 2024) and the *Imaging X-ray Polarimetry Explorer* (IXPE; Zhao et al. 2024; Ingram et al. 2024).

Probing the QPO's characteristics during a state transition is crucial to understand their origin and formation. Méndez et al. (2024) simultaneously fitted the PS and the Real and Imaginary parts of the cross spectra (CS) using a multi-Lorentzian model in different LMXBs: *GX 339–4*, *GRS 1915+105*, and during the soft-to-hard transition of *MAXI J1820+070*. Their analyses show the necessity to fit the Real and Imaginary parts of the CS, as some QPOs can be significant in the CS but not in the PS. In the soft energy band (below 1 keV), König et al. (2024) and Fogantini et al. (2025) performed a similar analysis on the High-mass X-ray binary (HMXB) *Cyg X-1* using *NICER* data. Despite the differences in the companion's mass, several of these sources (including *J1727*), exhibit a sudden jump in the phase lags and a coherence drop at a specific frequency, which can be attributed to an additional narrow Lorentzian visible only in the Imaginary part of the CS. This narrow Lorentzian is likely induced by the variability from the corona. Studies in the rising and decaying phases of the outburst reveal these features only arising during the decaying phase of the soft-to-hard transition (Alabarta et al. 2022; Ma et al. 2023; Bellavita et al. 2025),

suggesting the disk inner radius expansion, or feedback from the corona as their origin.

This work presents the first timing analysis of *J1727* in the soft-to-hard transition with *XMM–Newton* data, using the multi-Lorentzian decomposition of the PS and CS framework presented in Méndez et al. (2024). From the CS of two different energy bands, we derived the phase lags, which trace the phase angle in the complex Fourier plane of the cross vector for correlated signals (van der Klis et al. 1987; van der Klis 1989; Vaughan et al. 1997; Nowak et al. 1999a). The coherence function – quantifying the linear correlation between the two signals depending on the Fourier frequency (Vaughan & Nowak 1997) – is then calculated.

This paper is structured as follows: we present the data set in Section 2, the multi-Lorentzian model fitting of the PS and CS is presented in Section 3, and discussed in Section 4, alongside the phase lags and coherence fitting.

## 2. Data Sets

We observed *J1727* with the *XMM–Newton's European Photon Imaging Camera (EPIC)–PN spectrograph* (covering the 0.15 – 12 keV energy band; Jansen et al. 2001; Strüder et al. 2001) during the soft-to-hard transition (see Table A.1, PID 88500; Castro Segura 2020). The data were processed using the Science Analysis Software (SAS; Gabriel et al. 2004) pipeline from ESA. The calibrated photon event files for the *PN* camera were produced with *epproc*. We extracted, filtered for pile-up, and rebinned (0.1 s) the light curves using *evselect*, for all three observations. We defined Good Time Intervals (GTIs) to remove the telemetry gaps (see Fig. A.1), and computed the power density and cross spectra presented in section 3.

## 3. Analysis and results

Using the General High-Energy Aperiodic Timing Software (GHATS<sup>1</sup>), we calculated the PS in the 0.3–2 keV and 2–12 keV energy bands, and the cross spectra between those same two bands. We fixed the sampling time to 0.006 s ( $200\times$  the native instrumental resolution), which defines the Nyquist frequency at  $0.5/0.006 = 83.3$  Hz. Based on the typical length of the GTI segments allowed by the telemetry gaps, we set the interval length for computing the PS to  $2048 \times 0.006\text{s} \approx 12.3$  s, corresponding to a minimum frequency of  $\sim 0.08$  Hz. Consequently, the second observation (ObsID 0885000701) ended up with 641 segments against 1605 segments for the third observation (ObsID 0885000801). To increase the Signal to Noise Ratio at high frequencies, we logarithmically rebinned the PS and CS, by a factor of  $10^{0.01} \approx 1.023$ . The PS and CS were normalized to fractional rms units (van der Klis 1989). Poisson noise and cross-talk levels were estimated empirically from the 30–80 Hz frequency range, where no signal is detected, and subtracted from the PS and the Real part of the CS. Therefore, the PS and CS are fitted only up to 30 Hz. Using the PS and CS, we computed the phase lags and the coherence for all observations, then fitted with the X-Ray Spectral Fitting Package (Xspec; Arnaud 1996).

<sup>1</sup> [http://astrosat-ssc.iucaa.in/uploads/ghats\\_home.html](http://astrosat-ssc.iucaa.in/uploads/ghats_home.html)

**Table 1.** Best fitting parameters of the PS and CS for both observations in the soft-to-hard transition. “Comp” refers to the model components and L1-3 refer to the three fitted Lorentzians (defined in equations 1 for the PS and in equation 3 for the CS).

Epoch	Comp.	$\nu_0$ [Hz]	FWHM [Hz]	$Q = \frac{\nu_0}{\text{FWHM}}$	rmSPS, 0.3–2keV [%]	rmSPS, 2–12keV [%]	Phase lags [rad]
XMM2	L1	$0.26 \pm 0.01$	$1.13 \pm 0.02$	$0.23 \pm 0.01$	$16.38 \pm 0.08$	$25.5 \pm 0.2$	$0.010 \pm 0.005$
	L2	$2.59 \pm 0.04$	$1.25 \pm 0.14$	$2.07 \pm 0.23$	$3.5 \pm 0.2$	$6.3 \pm 0.7$	$0.70 \pm 0.05$
	L3	$3.48 \pm 0.24$	$5.75 \pm 0.30$	$0.60 \pm 0.05$	$4.5 \pm 0.2$	$15.0 \pm 0.6$	$0.26 \pm 0.03$
$\chi^2/\text{dof}$		910.58 / 699 $\approx$ 1.3					
XMM3	L1	$0.218 \pm 0.006$	$0.93 \pm 0.01$	$0.234 \pm 0.007$	$17.13 \pm 0.07$	$24.6 \pm 0.1$	$0.016 \pm 0.003$
	L2	$1.98 \pm 0.01$	$0.48 \pm 0.05$	$4.12 \pm 0.43$	$2.9 \pm 0.1$	$3.7 \pm 0.3$	$0.81 \pm 0.04$
	L3	$2.48 \pm 0.08$	$4.6 \pm 0.1$	$0.54 \pm 0.02$	$6.4 \pm 1.4$	$17.3 \pm 0.2$	$0.32 \pm 0.01$
$\chi^2/\text{dof}$		1338.33 / 699 $\approx$ 1.9					

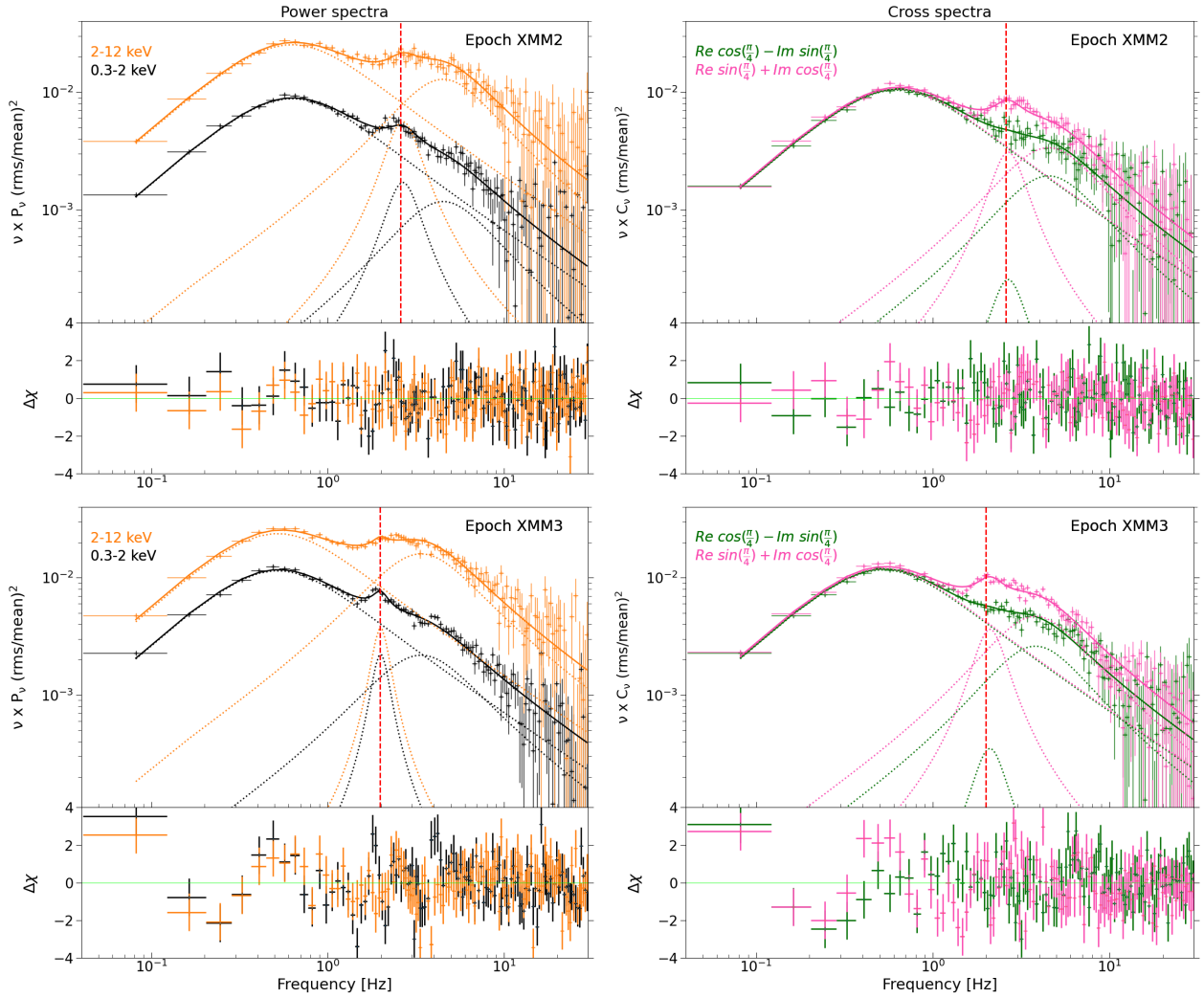


**Fig. 1.** *Left panel:* Power spectra of the second (top) and third (bottom) *EPIC-PN* observations of *Swift J1727.8–1613* in the 0.3–2 keV (black) and 2–12 keV (orange) energy bands. *Right panel:* Real (green) and Imaginary (pink) parts of the cross spectra of the same two observations using the 0.3–2 keV and 2–12 keV energy bands, rotated by 45° (see Section 3.2 for more details). The vertical red line shows the position of the central frequency  $\nu_0$  of the Imaginary QPO. The total model is shown with the continuous line and the individual Lorentzians are in dotted lines. Below each fit are the residuals defined as  $\Delta\chi = (\text{data} - \text{model})/\text{error}$ .

### 3.1. The power spectra

Unsurprisingly, no significant variability was observed in the PS of the first (soft state) observation. Therefore, this analysis focuses on the last two observations during the soft-to-hard transition. The PS were computed using GHATS and fitted in Xspec

with an additive multi-Lorentzian model for each observation (see Fig. 1). Following Méndez et al. (2024), the Lorentzians are assumed to be coherent between the two energy bands across the Fourier frequencies, but incoherent between each other. Thus,

the PS in two energy bands, x and y, can be defined as a sum of Lorentzians:

$$\begin{aligned} G_{xx}(\nu) &= \sum_{i=1}^3 G_{xx,i}(\nu) = \sum_{i=1}^3 A_i L(\nu; \nu_{0,i}, \Delta_i) \\ G_{yy}(\nu) &= \sum_{i=1}^3 G_{yy,i}(\nu) = \sum_{i=1}^3 B_i L(\nu; \nu_{0,i}, \Delta_i), \end{aligned} \quad (1)$$

with  $i = 1, 2, 3$  for the three Lorentzians,  $A_i$ ,  $B_i$  are the integrated power from zero to infinity of the Lorentzians, in respectively, band x and y,  $\nu_{0,i}$  is the central frequency for each individual Lorentzian and  $\Delta_i$  their full width at half maximum (FWHM). Since for each Lorentzian function we assume the coherence function to be  $\gamma_{xy,i}^2(\nu) = 1$  and the modulus square of the CS to be:  $|G_{xy}(\nu)|^2 = A_i B_i L^2(\nu; \nu_{0,i}, \Delta_i)$ , the former is then defined as:

$$\gamma_{xy}^2(\nu) = \frac{|G_{xy}(\nu)|^2}{G_{xx}(\nu)G_{yy}(\nu)}. \quad (2)$$

Table 1 gives the best-fitting parameters from the Xspec fitting with three Lorentzians for each observation. The central frequency  $\nu_0$  and the FWHM of the Lorentzians in the 2–12 keV energy band are linked to the values from the low energy band (0.3–2 keV). Only the fractional rms amplitude remains a free parameter in both bands. The quality factor  $Q$  is defined as the ratio between the central frequency of the QPO and the FWHM. The best fits using the multi-Lorentzian model give  $\chi^2 / \text{dof} \sim 1.3$  and  $\chi^2 / \text{dof} \sim 1.9$ , for the second and third observation, respectively. The model describes the data correctly in both cases, without prominent features in the residuals. Overall, the PS has a greater rms amplitude at higher energy, with a total rms of  $\sim 17\%$  in 0.3–2 keV versus  $\sim 30\%$  in 2–12 keV.

Additionally, the rms of the first and last Lorentzians (referred to as L1 and L3) increase in the 0.3–2 keV energy band as the outburst evolves from the second to the third observation: the rms goes from  $\sim 16.4\%$  to  $\sim 17.1\%$  for L1 and from  $\sim 4.5\%$  to  $\sim 6.4\%$  for L3. In the 2–12 keV energy band, the rms similarly increases for L3 but decreases for L1, from  $\sim 6.3\%$  to  $\sim 3.7\%$ . On the other hand, the rms amplitude of L2 decreases in both energy bands: from  $\sim 3.5\%$  to  $\sim 2.9\%$  in the 0.3–2 keV energy band and from  $\sim 6.3\%$  to  $\sim 3.7\%$  in the 2–12 keV energy band.

Furthermore, the central frequencies of the three Lorentzians shift toward lower frequencies as the source hardens, decreasing by  $\sim 16\%$ ,  $\sim 23\%$ , and  $\sim 28\%$  for L1, L2, and L3, respectively, between the second and third observation. The Lorentzians also become narrower, with a decrease in the FWHMs of  $\sim 18\%$ ,  $\sim 62\%$  and  $\sim 20\%$  between the second and third observation (see Table 1). As a result, as the source hardens, the quality factor of the second Lorentzian increases from 2.07 to 4.12, but decreases for L3 from 0.60 to 0.54. Parallely, the  $Q$  factor of L1 remains constant around 0.23 within the errors.

### 3.2. The Real and Imaginary parts of the cross spectrum

Following Méndez et al. (2024), the Real and Imaginary parts of the CS were fitted in a similar way as the PS, where they are decomposed into a linear combination of Lorentzians multiplied

by the phase lag dependency using the relation:

$$\begin{aligned} \Re[G_{xy}(\nu)] &= \sum_{i=1}^3 C_i L(\nu; \nu_{0,i}, \Delta_i) \cos(\Delta\phi_{xy,i}(\nu) + \pi/4) \\ \Im[G_{xy}(\nu)] &= \sum_{i=1}^3 C_i L(\nu; \nu_{0,i}, \Delta_i) \sin(\Delta\phi_{xy,i}(\nu) + \pi/4), \end{aligned} \quad (3)$$

with  $C = \sqrt{AB}$  and the frequency-dependent phase lags between the two signals is defined as:

$$\Delta\phi_{xy,i}(\nu) = \tan^{-1} \left( \frac{\Im[G_{xy,i}(\nu)]}{\Re[G_{xy,i}(\nu)]} \right) = g_i(\nu; p_{j,i}). \quad (4)$$

Here, we explicitly treat the phase lags of the  $i$ -th Lorentzian as a function of the parameters  $p_{j,i}$ . In the rest of the paper, we assume the phase lags of each Lorentzian to be constant with frequency:  $g_i(\nu; p_{j,i}) = \Delta\phi_i$ , where  $\Delta\phi_i$  is a parameter of the model. This is the constant phase lag model as defined in Méndez et al. (2024). The phase lags of J1727 are close to zero across the Fourier frequencies, thus, the amplitude of the Imaginary part of the CS is smaller than the Real part. Consequently, the cross vectors can be rotated by  $45^\circ$  to have comparable Real and Imaginary parts, enhancing more stable fits in Xspec, without impacting the best-fitting parameters (c.f. Méndez et al. 2024). Therefore, by multiplying the cross vector (decomposed into a Real and Imaginary part) by the rotation matrix, we calculated the Real and Imaginary parts of the CS as  $\Re[\cos(\pi/4)] - \Im[\sin(\pi/4)]$  and  $\Re[\sin(\pi/4)] + \Im[\cos(\pi/4)]$ , respectively. The central frequencies and FWHMs of the three Lorentzians in the CS are tied to those in the 0.3–2 keV band of the PS. Meanwhile, the normalization of the Real part of the CS is given by the parameter  $C$ , previously defined. Table 1 shows the best-fitting parameters of the phase lags of the CS between 0.3–2 keV and 2–12 keV. The fitted rotated Real (green) and rotated Imaginary (pink) parts of the CS are shown on the right panel of Fig. 1. Below 1.5 Hz, the rotated Real and Imaginary parts of the CS are overlapping in the two energy bands, for both observations. Above 1.5 Hz, the rotated Imaginary part of the CS in the 2–12 keV energy range is higher than the rotated Real part. A bump is observed in the rotated Imaginary part of the CS at  $\sim 3$  Hz, and is well-fitted by a narrow Lorentzian. In both observations, we identify a narrow Lorentzian in the PS and the CS with a stronger Imaginary component compared to the Real part. We name this QPO the “Imaginary QPO”, as first expressed by Méndez et al. (2024). While the rms of the Imaginary QPO stays more or less constant when the system hardens, the Real part’s increases.

### 3.3. The phase lags and coherence

The last column of Table 1 shows the best-fitting parameters for the phase lags. The phase lags of the three Lorentzians increase by  $\sim 37\%$ ,  $\sim 13\%$ , and  $\sim 19\%$  (for L1, L2, and L3, respectively), between the second and third observation. From the PS and CS fits, we derive a model of the phase lags and the coherence, calculated in the same energy bands as the power and cross spectra. Fig. 2 displays the phase lags (top panel) and the coherence (bottom panel) for the two observations, together with the predicted model. Below 1 Hz, the phase lags are on average constant around  $\sim 0$  rad, with a small excess around  $\sim 0.2$  Hz and  $\sim 0.5$  Hz, significant at the 68% confidence level. Then, the phase lags reach a maximum value at the Imaginary QPO frequency, marked by the vertical dotted red line, and stabilize to a higher constant value around  $\sim 1.8$  rad after that, for both observations.



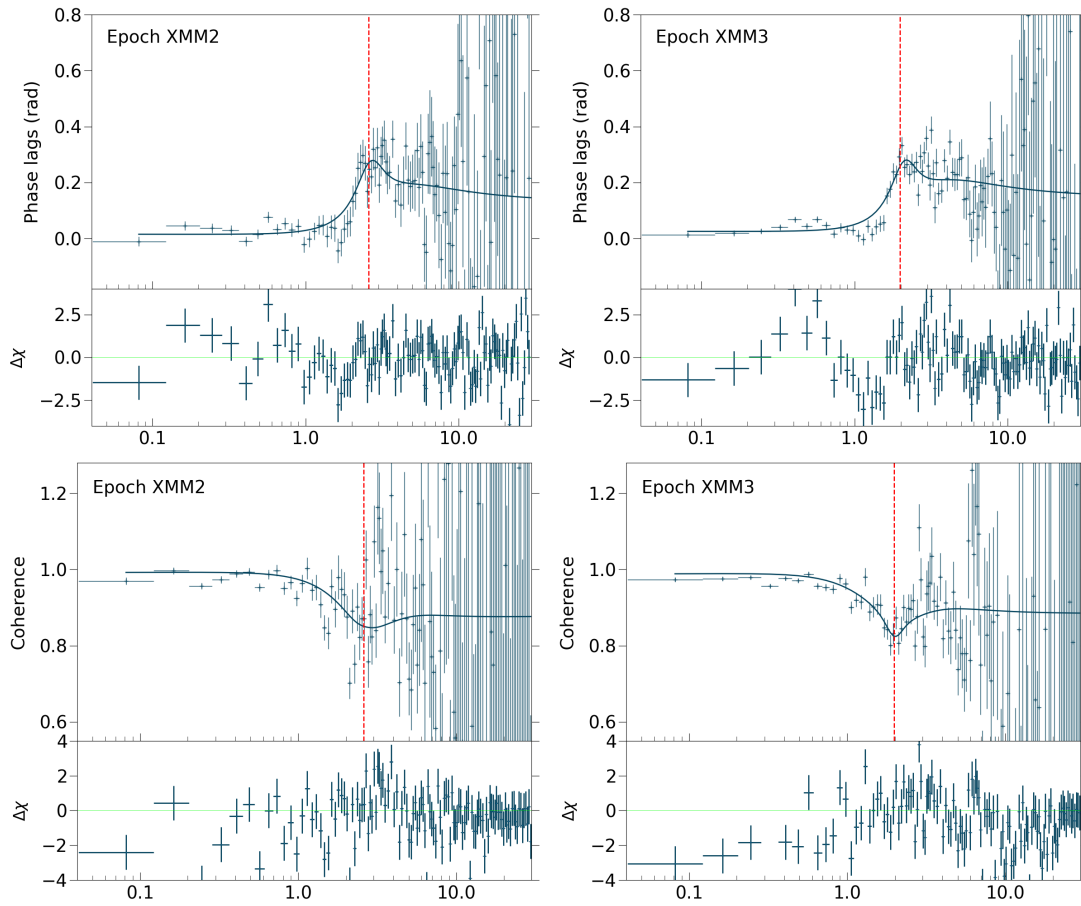


**Fig. 2.** The phase lags in radian (top) and the coherence function (bottom) for the second (left panel) and third (right panel) *EPIC-PN* observation of *Swift J1727.8–1613*. The continuous lines show the predicted model from the fits of the PS and CS represented in Fig. 1. The bottom panels show the residuals defined as (data-model)/error. The red dotted vertical line indicates the central frequency of the Imaginary QPO for each observation.

However, in the second observation, the phase lags are narrower and are dominated by the uncertainties above 7 Hz for both observations.

While the phase lags increase at the Imaginary QPO’s central frequency, the coherence drops. Below 1 Hz, the average coherence value is around  $\sim 1$ , it then drops to  $\sim 0.8$  at the frequency of the “Imaginary QPO” and remains constant around  $\sim 0.9$  after the dip. Similarly to the phase lags, the residuals drop significantly around  $\sim 0.5$  Hz, aligning with a slight decrease in the coherence. These features suggest the presence of an additional component contributing to the variability at low frequency. However, we did not add another Lorentzian to account for this component in our model, as we aim to fit the prominent variable components with as few Lorentzians as possible.

### 3.4. The energy dependence of the QPO lags and rms amplitude

To analyze the QPO lags and rms amplitude energy dependence, we computed the Fast Fourier Transforms (FFTs) and CS for each narrow energy band relative to the full (0.3–12 keV) energy band, at the Imaginary QPO frequency. The data were then fitted using the multi-Lorentzian model previously defined, with central frequencies and FWHMs fixed to the best fit values listed in Table 1. Fig. 3 shows the energy dependence of the fractional rms (top) and the phase lags (bottom). In Epoch XMM2, the rms amplitude of the QPO increases from 2% to 9.5% between 0.5 keV and 8 keV. In Epoch XMM3, the rms amplitude in-

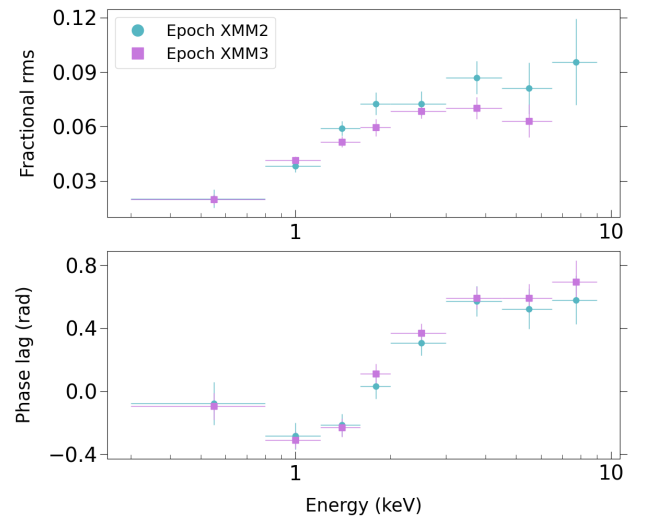


**Fig. 3.** Energy dependence of the fractional rms (top) and the phase lags (bottom) of the Imaginary QPO for the second (blue circles) and third (purple squares) *EPIC-PN* observations of *Swift J1727.8–1613*.

creases from 2% to  $\sim 7\%$  between 0.5 keV and 5.5 keV. The higher energy bands being poorly constrained, with errors significant up to  $3\sigma$ , we do not consider them in the analysis. On the other hand, the phase lags reach a minimum value at 1 keV. In Epoch XMM2, the phase lags decrease from  $\sim -0.08$

rad to  $\sim -0.28$  rad between 0.5 keV and 1 keV and increase again from  $\sim -0.21$  rad at 1.2 keV to  $\sim -0.58$  rad at 8 keV. In Epoch XMM3, a similar behaviour is observed with a decrease from  $\sim -0.09$  rad at 0.5 keV to a minimum value of  $\sim -0.31$  rad at 1 keV, increasing above 1 keV.

## 4. Discussion and conclusions

In section 3, we showed that the *XMM EPIC-PN* data of the BH LMXB *Swift J1727.8–1613* reveal the presence of a Type-C QPO in the soft-to-hard transition. While the characteristic Lorentzians' frequencies shift to lower values as the source hardens, the phase lags increase and the coherence function drops at the QPO frequency, reinforcing the possible cause-to-effect relationship between the Type-C QPO and the features observed in the lags and the coherence. An in-depth discussion is provided below.

### 4.1. The Type-C QPO

We identify a narrow Lorentzian in the PS characterized by a higher rms amplitude in the Imaginary part than in the Real part of the CS, where the Real counterpart's rms increases between the second and the third observation. The origin of the Imaginary QPO is still unclear: In *Cyg X-1*, König et al. (2024) suggested a beat between the two broad Lorentzians, which could create a third component causing the QPO, often observed in the PS, whereas Méndez et al. (2024) argue that it comes from an independent phenomenon. Nonetheless, the Imaginary QPO of the source seems to correspond to the QPO observed in the PS.

The QPO identified in *J1727*'s PS and CS has a central frequency at  $\sim 2.6$  Hz in the second observation, shifting to  $\sim 2$  Hz in the third observation. Furthermore, the total rms is  $\sim 17\%$  and  $\sim 18\%$  in the 0.3–2 keV energy band, for the second and last observation, respectively, reaching  $\sim 30\%$  in the 2–12 keV energy band for both observations. Given *J1727*'s brightness and high-rms LFQPO in both the PS and CS, we classify the LFQPO, observed in the soft-to-hard transition, as a Type-C QPO (Motta et al. 2011). In the rms–intensity diagram for black hole transients defined by Muñoz-Darias et al. (2011), the source would be close to the hard line, the designated position of Type-C QPOs. However, the  $Q$  factor values for *J1727* are lower than those usually observed for Type-C QPOs ( $\sim 7$ –10). Low  $Q$  factors in Type-C QPOs were also observed in *MAXI J1348–630* (Alabarta et al. 2022) and *MAXI J1820+070* (Ma et al. 2023), ranging between 0.2 and 7.

On the other hand, as the system hardens, the QPO moves to lower frequencies. This frequency shift – probably induced by the Comptonizing plasma dominating the emission in the hard state – has previously been observed in other XBs (*MAXI J1820+070*; Méndez et al. 2024; Bellavita et al. 2025, and *Cyg X-1*; König et al. 2024; Fogantini et al. 2025). Furthermore, during the soft-to-hard transition of *MAXI J1348–630*, Alabarta et al. (2025) interpreted the QPO frequency shifting to lower frequencies as indicative of coronal expansion. In the case of *GRS 1915+105*, Méndez et al. (2022) and García et al. (2022) explain the frequency shift by a perpendicular contraction of the corona with respect to the accretion disk. Thus, the frequency shift suggests a geometric change in the corona.

Additionally, observed in the soft-to-hard transition, the Type-C QPO can be attributed to the expansion of the truncated disk inner radius or by feedback processes from the corona (Bellavita et al. 2022). The Lense-Thirring precession, due to the inner

accretion flow precessing with respect to the thermal disk (see Ingram et al. 2009), has also been proposed as the origin of Type-C QPOs in XBs, supported by studies showing a tight anti-correlation between the outer radius of the Comptonizing region and  $\nu_{\text{QPO}}$  (Kubota et al. 2024). However, the analysis of *GRS 1915+105* by Nathan et al. (2022) reveals an inner disk radius too small and a reprocessing time too large to support this model.

Apart from the Type-C QPO, the broadband Lorentzians, L1 and L3, similarly shift to lower frequencies as the source hardens. However, in the 0.3–2 keV energy band, as the source transitions, their rms amplitude increases, unlike that of the Type-C QPO. This behaviour was previously observed in *GX 339-4* (Muñoz-Darias et al. 2011). In the 2–12 keV hard band, for a harder emission, the rms increases for L3 but decreases for L1. Thus, as suggested by Bellavita et al. (2025), the two broad Lorentzians seem independent from each other and might come from independent variability processes than the QPO's. König et al. (2024) support this assumption proposing L1 to come from the accretion disk and modulated by the Comptonization, and L3 to be associated with the Comptonized medium. On the other hand, Wilkinson & Uttley (2009) link the L1 variability to an unstable accretion flow in the disk (though they reached that conclusion by fitting the covariance spectrum with the same model as the time-averaged one, which only holds if only the overall normalization of the model varies).

### 4.2. Phase lags jump

At the QPO frequency, the phase lags reach a maximum, also called the “cliff”, and was previously observed in other XBs (Méndez et al. 2024; Bellavita et al. 2025). Yet, before and after the QPO frequency, the phase lags remain constant around  $\sim 0$  rad and  $\sim 0.18$  rad, respectively, for both observations, with a sharper “cliff” in the third observation. In the frequency range in which one Lorentzian dominates the PS, the phase lags remain on average constant, where each Lorentzian has its own lags, potentially due to separate resonances (Méndez et al. 2024). On the contrary, at the intersection of the two Lorentzians, the phase lags transition from one constant value to another one. Nowak et al. (1999b) attributed this difference to the total phase lags at each Fourier frequency being equal to the average phase lags of the individual Lorentzians, weighted by the product of their amplitudes in the two energy bands at which they are calculated (defined as the small-angle approximation of equation 9 in Méndez et al. 2024). As a result, the phase lags are constant over a given frequency range when the Fourier amplitudes of one Lorentzian dominate.

Besides, the “cliff” is not observed in the hard energy bands. Similarly observed in the rising phase of the outburst of *J1727*, Yu et al. (2024) did not find the phase lags jump in the 1–10 keV and 25–150 keV energy bands, but still detected it in the soft energy bands, 1–2 keV and 2–10 keV, this may suggest that soft energies are essential to observe the phase-lag jump, regardless of the transition direction. Perhaps indicating that the QPO may originate from variations in a soft component linked to the accretion disk. Furthermore, as the source hardens, the Comptonization-driven variability from the corona intensifies and may introduce additional variability in the accretion disk.

### 4.3. Coherence drop

While the phase lags reach a maximum value at the QPO frequency, the coherence reaches a local minimum (König et al. 2024; Méndez et al. 2024; Bellavita et al. 2025; Fogantini et al. 2025), with different “plateau” values before and after the QPO frequency. Before the drop, the constant coherence around  $\sim 1$  indicates the physical interconnection between the variability in the disk and the corona (König et al. 2024). After the drop, the constant value around  $\sim 0.9$  points toward an increasing variability of the corona at the QPO frequency. In order to test this assumption, we fitted the PS, CS, phase lags, and coherence with only two Lorentzians instead of three. We obtained worst fits, with a  $\chi^2/\text{dof} \sim 1.5$  for the second observation, and a  $\chi^2/\text{dof} \sim 2.4$  for the third observation. In the residuals of the PS and CS, we identified a broad Gaussian-shaped component between  $3\sigma$  and  $4\sigma$  significant for the phase lags and coherence fits, indicating a missing component in the model. Consequently, minimum three Lorentzians (i.e. including a narrow one), are required for the model to correctly fit the PS, CS, phase lags “cliff” and coherence drop of J1727, similarly to MAXI J1820+070 (Bellavita et al. 2025; Fogantini et al. 2025) and Cyg X-1 (König et al. 2024). Ultimately, the drop in coherence might come from a weaker interaction between the large corona and the accretion disk at the QPO frequency as the transition goes (Alabarta et al. 2025), explaining the sharper coherence drop and phase lags “cliff” observed in the last observation (see Fig. 2).

Overall, the phase-lags jump and the coherence drop seem to be generated by low-energy variations from a soft component in the accretion disk at the Type-C QPO frequency, induced by variations in the corona geometry (Méndez et al. 2022; Alabarta et al. 2025). Only observed in the decaying phase of the outburst (Méndez et al. 2024; Alabarta et al. 2025; König et al. 2024; Bellavita et al. 2025; Fogantini et al. 2025), these features are significant at low X-ray flux in the soft-to-hard transition. Moreover, the phase lags and coherence of J1727 show a significant excess at  $\sim 0.4$  Hz and  $\sim 3$  Hz – previously observed in other sources, with a different instrument (Méndez et al. 2024; König et al. 2024) – confirming a physical origin of the signal.

### 4.4. QPO energy dependence

In J1727, the QPO frequency does not depend on energy, it stays constant in the 0.3–2 keV compared to the 2–12 keV energy bands. At the QPO frequency ( $\sim 2$  Hz), the fractional rms continually increases with energy, due to the decreasing contribution of the disk at higher energies (as observed in other sources; Alabarta et al. 2022, 2025; Fogantini et al. 2025; Bellavita et al. 2025). Parallely, the phase lags reach a minimum value around 1 keV for J1727, around 1.6 keV for MAXI J1348–630 (Alabarta et al. 2025) and around 1.5 keV for MAXI J1820+070 (Ma et al. 2023), staying constant  $\geq 4$  keV. The U-shaped energy lags could be explained by a fraction of the cold seed photons from the accretion disk entering the extended corona in the horizontal direction, resulting in a significant drop in the phase lags (Liao et al. 2024; Alabarta et al. 2025; Bellavita et al. 2025). Furthermore, as the source hardens, Bellavita et al. (2025) show a more prominent drop in the phase lags.

## 5. Summary

To summarize, we identified a Type-C QPO in the soft-to-hard transition of the BH LMXB Swift J1727.8–1613, significant in both the PS and CS. As the source transitions from the soft to

the hard state, the QPO frequency shifts to lower frequencies, the broadband fractional rms amplitude in the 0.3–2 keV energy band increases, and the rms covariance of the QPO decreases. At the QPO frequency, the phase lags increase and the coherence function drops, probably due to variations in the corona geometry. Moreover, XMM-Newton’s unprecedented detection of these features in the elusive decaying phase of the outburst support a physical origin of the low-frequency excess observed in the lags and coherence. Follow-up modelling of this source may help understand the relative strength of the Type-C QPO in the Imaginary component of the CS.

**Acknowledgements.** Research is based on observations obtained with XMM-Newton, an ESA science mission with instruments and contributions directly funded by ESA Member States and NASA. M.B. acknowledges the support from GAUK project No. 102323. J.S. thanks GACR project 21-06825X for the support. NCS acknowledges support from the Science and Technology Facilities Council (STFC) grant ST/X001121/1. FG acknowledges support from PIBAA 1275 and PIP 0113 (CONICET). FG was also supported by grant PID2022-136828NBC42 funded by the Spanish MCIN/AEI/10.13039/501100011033 and ERDF A way of making Europe. MM acknowledges the research programme Athena with project number 184.034.002, which is (partly) financed by the Dutch Research Council (NWO). We thank Santiago del Palacio for valuable discussion and comments.

## Data Availability

The data underlying this article is publicly available in: *Pan-STARRS* <https://archive.stsci.edu/panstarrs/> and *AAVSO* <https://www.aavso.org>. Remaining data will be shared on reasonable request to the corresponding author.

## References

- Alabarta, K., Méndez, M., García, F., et al. 2025, *ApJ*, 980, 251
- Alabarta, K., Méndez, M., García, F., et al. 2022, *MNRAS*, 514, 2839
- Arnaud, K. A. 1996, in *Astronomical Society of the Pacific Conference Series*, Vol. 101, *Astronomical Data Analysis Software and Systems V*, ed. G. H. Jacoby & J. Barnes, 17
- Bellavita, C., García, F., Méndez, M., & Karpouzas, K. 2022, *MNRAS*, 515, 2099
- Bellavita, C., Méndez, M., García, F., Ma, R., & König, O. 2025, *A&A*, 696, A128
- Belloni, T., Homan, J., Casella, P., et al. 2005, *A&A*, 440, 207
- Belloni, T., Psaltis, D., & van der Klis, M. 2002, *ApJ*, 572, 392
- Bollemeijer, N., Uttley, P., Buisson, D., et al. 2023, *The Astronomer’s Telegram*, 16247, 1
- Burridge, B. J., Miller-Jones, J. C. A., Bahramian, A., et al. 2025, *arXiv e-prints*, arXiv:2502.06448
- Casella, P., Belloni, T., Homan, J., & Stella, L. 2004, *A&A*, 426, 587
- Casella, P., Belloni, T., & Stella, L. 2005, *ApJ*, 629, 403
- Castro Segura, N. 2020, *Outflow Legacy Accretion Survey: unveiling the wind driving mechanism in BHXRBs*, XMM-Newton Proposal ID #88500
- Castro-Tirado, A. J., Sanchez-Ramirez, R., Caballero-Garcia, M. D., et al. 2023, *The Astronomer’s Telegram*, 16208, 1
- Chatterjee, K., Mondal, S., Singh, C. B., & Sugizaki, M. 2024, *ApJ*, 977, 148
- Dichiera, S., Kennea, J. A., Page, K. L., et al. 2023, *GRB Coordinates Network*, 34542, 1
- Done, C., Gierliński, M., & Kubota, A. 2007, *A&A Rev.*, 15, 1
- Drachis, P. A., Miller, J. M., Homan, J., et al. 2023, *The Astronomer’s Telegram*, 16219, 1
- Dunn, R. J. H., Fender, R. P., Körding, E. G., Belloni, T., & Cabanac, C. 2010, *MNRAS*, 403, 61
- Fender, R. P., Belloni, T. M., & Gallo, E. 2004, *MNRAS*, 355, 1105
- Fogantini, F. A., García, F., Méndez, M., König, O., & Wilms, J. 2025, *arXiv e-prints*, arXiv:2503.03078
- Frank, J., King, A., & Raine, D. J. 2002, *Accretion Power in Astrophysics: Third Edition*
- Gabriel, C., Denby, M., Fyfe, D. J., et al. 2004, in *Astronomical Society of the Pacific Conference Series*, Vol. 314, *Astronomical Data Analysis Software and Systems (ADASS) XIII*, ed. F. Ochsenbein, M. G. Allen, & D. Egret, 759
- García, F., Karpouzas, K., Méndez, M., et al. 2022, *MNRAS*, 513, 4196

- García, F., Mendez, M., & Karpouzas, K. 2021, in 43rd COSPAR Scientific Assembly. Held 28 January - 4 February, Vol. 43, 1695
- Giannios, D. & Spruit, H. C. 2004, A&A, 427, 251
- Hirsch, M., Pottschmidt, K., Smith, D. M., et al. 2020, A&A, 636, A51
- Homan, J., Wijnands, R., van der Klis, M., et al. 2001, The Astrophysical Journal Supplement Series, 132, 377
- Ingram, A., Bollemeijer, N., Veledina, A., et al. 2024, ApJ, 968, 76
- Ingram, A., Done, C., & Fragile, P. C. 2009, MNRAS, 397, L101
- Jansen, F., Lumb, D., Altieri, B., et al. 2001, A&A, 365, L1
- König, O., Mastroserio, G., Dauser, T., et al. 2024, A&A, 687, A284
- Kubota, A., Done, C., Tsurumi, K., & Mizukawa, R. 2024, MNRAS, 528, 1668
- Liao, J., Chang, N., Cui, L., et al. 2024, arXiv e-prints, arXiv:2410.06574
- Ma, R., Méndez, M., García, F., et al. 2023, MNRAS, 525, 854
- Ma, X., Tao, L., Zhang, S.-N., et al. 2021, Nature Astronomy, 5, 94
- Mastichiadis, A., Petropoulou, M., & Kylafis, N. D. 2022, A&A, 662, A118
- Mata Sánchez, D., Muñoz-Darias, T., Armas Padilla, M., Casares, J., & Torres, M. A. P. 2024, A&A, 682, L1
- Matsuoka, M., Kawasaki, K., Ueno, S., et al. 2009, PASJ, 61, 999
- Méndez, M., Karpouzas, K., García, F., et al. 2022, Nature Astronomy, 6, 577
- Méndez, M., Peirano, V., García, F., et al. 2024, MNRAS, 527, 9405
- Mihara, T., Kawai, N., Yoshida, A., et al. 2002, in Society of Photo-Optical Instrumentation Engineers (SPIE) Conference Series, Vol. 4497, X-Ray and Gamma-Ray Instrumentation for Astronomy XII, ed. K. A. Flanagan & O. H. W. Siegmund, 173–186
- Mihara, T., Nakajima, M., Sugizaki, M., et al. 2011, PASJ, 63, S623
- Mondal, S., Basu, P., & Chakrabarti, S. K. 2009, MNRAS, 396, 1038
- Motta, S., Muñoz-Darias, T., Casella, P., Belloni, T., & Homan, J. 2011, MNRAS, 418, 2292
- Muñoz-Darias, T., Motta, S., & Belloni, T. M. 2011, MNRAS, 410, 679
- Nathan, E., Ingram, A., Homan, J., et al. 2022, MNRAS, 511, 255
- Negoro, H., Serino, M., Nakajima, M., et al. 2023, The Astronomer’s Telegram, 16205, 1
- Norris, J. P. & Wood, K. S. 1987, ApJ, 312, 732
- Nowak, M. A., Vaughan, B. A., Wilms, J., Dove, J. B., & Begelman, M. C. 1999a, ApJ, 510, 874
- Nowak, M. A., Wilms, J., & Dove, J. B. 1999b, ApJ, 517, 355
- Palmer, D. M. & Parsotan, T. M. 2023, The Astronomer’s Telegram, 16215, 1
- Podgorný, J., Svoboda, J., Dovčiak, M., et al. 2024, A&A, 686, L12
- Psaltis, D., Belloni, T., & van der Klis, M. 1999, ApJ, 520, 262
- Rawat, D., Méndez, M., García, F., & Maggi, P. 2025, arXiv e-prints, arXiv:2504.06705
- Remillard, R. A. & McClintock, J. E. 2006, ARA&A, 44, 49
- Shakura, N. I. & Sunyaev, R. A. 1973, A&A, 24, 337
- Stella, L. & Vietri, M. 1998, ApJ, 492, L59
- Stella, L., Vietri, M., & Morsink, S. M. 1999, ApJ, 524, L63
- Strüder, L., Briel, U., Dennerl, K., et al. 2001, A&A, 365, L18
- Sugizaki, M., Mihara, T., Serino, M., et al. 2011, PASJ, 63, S635
- Svoboda, J., Dovčiak, M., Steiner, J. F., et al. 2024, ApJ, 966, L35
- Tagger, M. & Pellat, R. 1999, A&A, 349, 1003
- Titarchuk, L. & Fiorito, R. 2004, ApJ, 612, 988
- van der Klis, M. 1989, ARA&A, 27, 517
- van der Klis, M., Hasinger, G., Stella, L., et al. 1987, ApJ, 319, L13
- Vaughan, B. A. & Nowak, M. A. 1997, ApJ, 474, L43
- Vaughan, B. A., van der Klis, M., Méndez, M., et al. 1997, ApJ, 483, L115
- Veledina, A., Muleri, F., Dovčiak, M., et al. 2023, ApJ, 958, L16
- Vernet, J., Dekker, H., D’Odorico, S., et al. 2011, A&A, 536, A105
- Weisskopf, M. C., Soffitta, P., Baldini, L., et al. 2022, Journal of Astronomical Telescopes, Instruments, and Systems, 8, 026002
- Wijnands, R. & van der Klis, M. 1998, The Astronomer’s Telegram, 17, 1
- Wilkinson, T. & Uttley, P. 2009, MNRAS, 397, 666
- Yu, W., Bu, Q.-C., Zhang, S.-N., et al. 2024, MNRAS, 529, 4624
- Zdziarski, A. A., Gierliński, M., Mikołajewska, J., et al. 2004, MNRAS, 351, 791
- Zhao, Q.-C., Tao, L., Li, H.-C., et al. 2024, ApJ, 961, L42



## Appendix A:

This data set is part of a multiwavelength observational campaign with Epochs defined by the optical observations from the *Very Large Telescope (VLT)*, performed with the *X-Shooter spectrograph* (Vernet et al. 2011), see Castro Segura et al. in preparation.

**Table A.1.** *XMM–Newton EPIC-PN* observation log of *Swift J1727.8–1613*.

Epochs	ObsID	Date	State	Exposure time [ks]
XMM1	0885000401	2024-02-26T14:20:50	high/soft	61
XMM2	0885000701	2024-03-25T01:42:16	soft-to-hard transition	20
XMM3	0885000801	2024-03-27T12:14:55	soft-to-hard transition	50

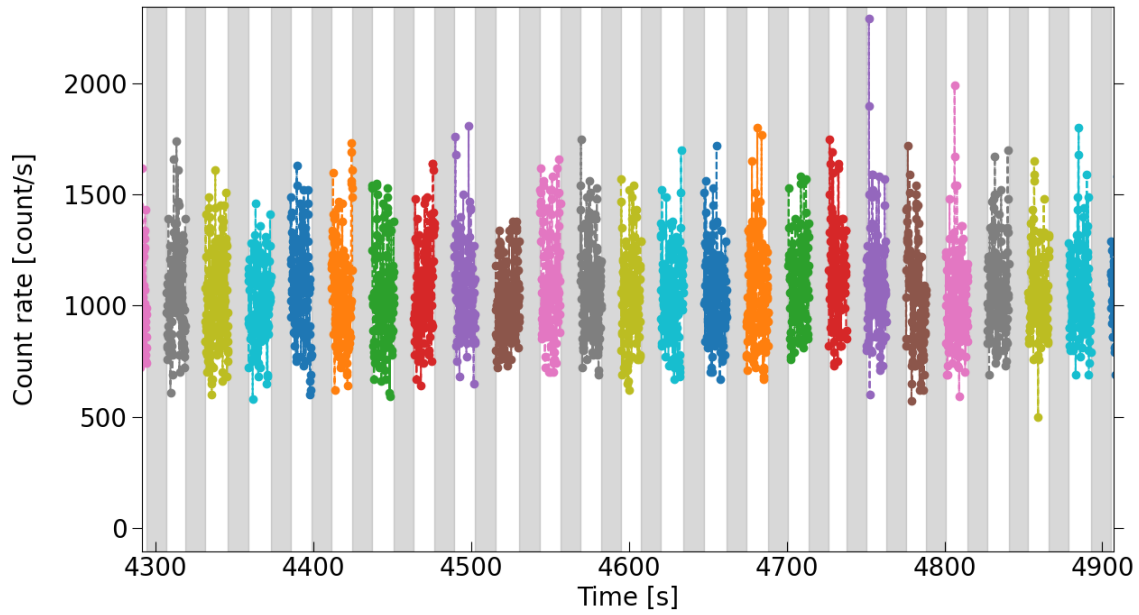


**Fig. A.1.** Zoomed *XMM EPIC-PN* light curves of *Swift J1727.8–1613* in the 0.2–12 keV energy range, with a binsize of 0.1 s for the second observation (Epoch XMM2). The shaded regions delimit the telemetry gaps and the colored data points are the Good Time Intervals (GTIs).

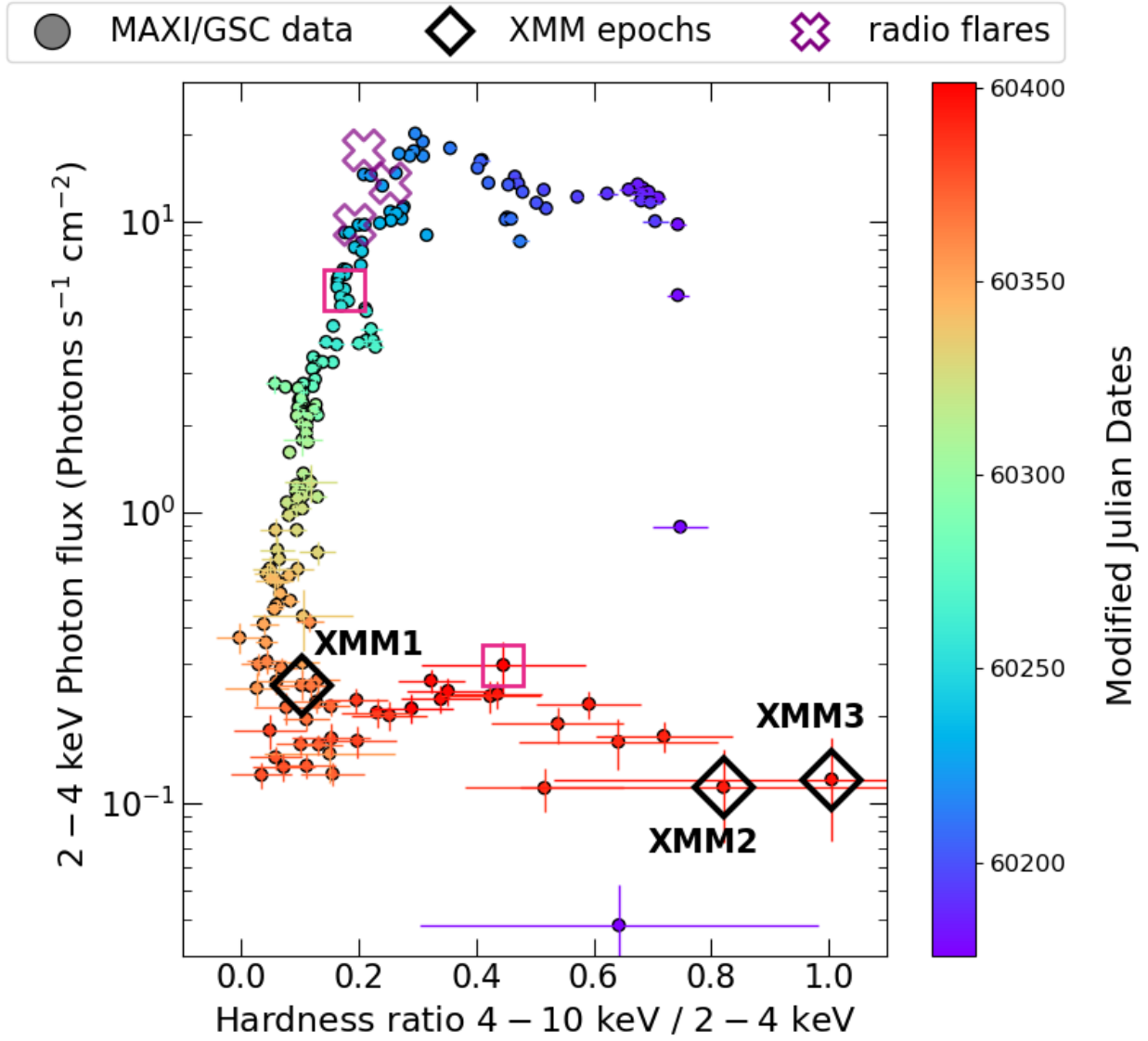


**Fig. A.2.** Hardness intensity diagram (HID) of *Swift J1727.8-1613* from the 2023 outburst. The photon fluxes are derived from the *MAXI/GSC* instrument with a bin size of 1 day from the "on-demand process" archives. The hardness ratio is defined as the photon flux ratio in the 4–10 keV over the photon flux in the 2–4 keV energy band. The pink squares indicate the beginning of the radio flaring period of the source and when the radio flux remains constant around 0.8 mJy (see radio monitoring of the source from Hughes et al. submitted), and the purple crosses indicate the position of the three radio flares.

Fig. A.2 shows the hardness intensity diagram (HID) of *Swift J1727.8-1613* since the start of the 2023 outburst. The light curves were obtained from the *Monitor of All-sky X-ray Image's* (*MAXI*; Matsuoka et al. 2009) *Gas Slit Camera* (*GSC*; 2–30 keV; Mihara et al. 2002; Sugizaki et al. 2011; Mihara et al. 2011), in the 2–10 keV energy band, and the *MAXI* "on-demand process" archives<sup>2</sup>. The position of the source in the HID during the *XMM EPIC-PN* observations are shown in black diamonds. The hardness ratio (HR) is defined as the ratio of the photon flux in the 4–10 keV energy band to that in the 2–4 keV energy band. While the pink squares indicate the beginning of the radio flaring period of the source and when the radio flux remains constant around 0.8 mJy (see radio monitoring of the source from Hughes et al. submitted), the purple crosses highlight the position of the three radio flares within the flaring period.

<sup>2</sup> <http://maxi.riken.jp/mxondem>